Ceramics International 45 (2019) 8333–8344

Contents lists available at ScienceDirect

Ceramics International

journal homepage: www.elsevier.com/locate/ceramint

Thermal diffusivity and microstructure of spark plasma sintered TiB_2–SiC–Ti composite

Mohammad Vajdi[a], Farhad Sadegh Moghanlou[a], Zohre Ahmadi[a], Amir Motallebzadeh[b], Mehdi Shahedi Asl[a,*]

[a] Department of Mechanical Engineering, University of Mohaghegh Ardabili, Ardabil, Iran
[b] Koc University Surface Science and Technology Center, Istanbul, Turkey

ARTICLE INFO

Keywords:
TiB_2–SiC
Titanium dopant
Spark plasma sintering
Thermal diffusivity
Microstructure
Finite element method

ABSTRACT

This work investigates the microstructural development, thermal properties and phase evolution of spark plasma sintered TiB_2–SiC–Ti (TST) ceramic composite. A fully dense TiB_2–30 vol% SiC composite, doped with 5 wt% Ti, was sintered by spark plasma at 1900 °C for 6 min under 35 MPa pressure in vacuum. The XRD analysis and thermodynamic assessments verified the in-situ synthesis of TiB, TiC and $TiSi_2$ compounds during the sintering process due to the chemical reaction of Ti additive with the SiC reinforcement. The TST composite showed higher thermal conductivity than the monolithic TiB_2 at low temperatures, however, a reverse trend was observed at higher temperatures. The governing equation of heat diffusion through a cutting tool, made of monolithic TiB_2 and TST, was solved by finite element method and the temperature distribution was obtained. The results showed that TST composite has lower value of maximum temperature compared to the reported values for WC. Cutting tools with lower temperatures result in higher accuracy and more tool lifespan.

1. Introduction

Ultrahigh temperature ceramics (UHTCs) are identified by their melting temperatures in excess of 3000 °C which can confront in extreme environments as structural materials. Several transition metal carbides, nitrides and diborides belong to this category [1–8]. Titanium diboride (TiB_2) is a member of UHTCs with exceptional properties. Its excellent combination of properties including high melting point, low specific weight, excellent electrical and thermal conductivity, good thermal shock resistance, relatively low coefficient of thermal expansion, good wettability with some liquid metals, considerable chemical inertness and stability, good machinability using electrical discharge machining, high corrosion resistance to some molten salts, high elastic modulus, hardness and abrasion resistance are attributed to the structure of TiB_2. TiB_2 has attained different industrial applications in corrosion and wear resistance parts, conductive coatings, cutting tools, crucibles, heating elements and sensors, control rods, cathode materials in aluminum refining and electrodes in metal smelting [9–19].

Densification of TiB_2-based composites is a challenging task due to the low volume self-diffusion coefficient and covalent bonding of diboride ceramics as well as the presence of surface oxide films on the powder particles [20]. Several densification routes have been used for fabrication of TiB_2 ceramics such as pressureless sintering (PS), hot pressing (HP) and spark plasma sintering (SPS). SPS is a newly developed sintering method to manufacture the UHTCs at lower temperatures compared with HP and PS [21–32]. Adding SiC as a reinforcement not only promotes the oxidation resistance of TiB_2 through the formation of a borosilicate protective layer [33–35], but also lessens the growth grains of TiB_2 matrix which leads to the enhancement of mechanical properties [36].

Despite mechanical properties importance in composites, especially in cutting tools, thermal properties have a considerable effect on their performance [37]. Temperature distribution (a function of thermal diffusivity, thermal conductivity and heat flux entered the specimen) can affect the deformation and accuracy of cutting tools. Excessive temperature has a direct effect on the tool lifespan and related operational costs. Moreover, high temperatures cause thermal stress and subsequent strains which affect the workpiece quality. Having information about temperature distribution through the tools makes it possible to have proper insight on designing of machining processes like choosing tool materials and cooling techniques which result in workpiece quality improvement [38].

Ceramics can be considered as wear-resistant parts in different applications [39], hence, temperature distribution gets important to

* Corresponding author.
E-mail address: shahedi@uma.ac.ir (M. Shahedi Asl).

https://doi.org/10.1016/j.ceramint.2019.01.141
Received 31 December 2018; Received in revised form 18 January 2019; Accepted 19 January 2019
Available online 24 January 2019

determine the wear resistance. The higher value of the thermal diffusivity, the more uniform temperature distribution in the heated bulk [40]. Thermal stresses as a result of high temperature gradient play a crucial rule on the failure of tool and final quality of the product. Therefore, many authors have paid attention to determination of thermal property of composites such as thermal conductivity, thermal diffusivity and thermal expansion [41].

Raju et al. [39] added $MoSi_2$ particles to TiB_2 ceramic and studied the high temperature heat diffusivity and electrical resistivity. The sample was manufactured by hot pressing and at the temperatures up to 1000 °C, heat diffusivity was measured by laser flash technique. Results showed that when the temperature increases, heat conductivity slightly increases up to 200 °C and then decreases [39]. Todorovic et al. [42] investigated the electrical resistivity of TiB_2 thin films. The films of TiB_2 was manufactured in the size of 9–450 nm. Post manufacturing process of rapid thermal annealing used to change the electrical resistivity of the thin films. They reported that the resistivity of TiB_2 films varied between 267 and 1820 μΩ cm as a function of thickness. While after annealing, because of grain growth through polycrystalline recrystallization, the resistivity varied from 267 to 16 μΩ cm. They found that the density of films and annealing temperature have great effects on resistivity which decreases with applying higher annealing temperatures [42].

Thermal conductivity of porous ZrB_2 ceramic was investigated by Yuan et al. [43]. The thermal diffusivity was measured and the thermal conductivity was calculated knowing the density and heat capacity of material. Porous ZrB_2 ceramic, with 21% porosity, was tested for thermal conductivity and with increasing the temperature, a trend of increase, decrease and increase again was observed.

Effect of TiB_2 additive (up to 30 wt%) on hot pressed ZrB_2 ceramic was studied by Chakraborty et al. [44]. The addition of TiB_2 particles resulted in higher grain boundary thermal resistance and reduced the thermal conductivity of the composite with respect to the monolithic ZrB_2. Thermal and mechanical properties of TiC ceramics was studied by Babapoor et al. [45]. They measured the thermal conductivity of TiC by the transient hot wire method. The effect of sintering temperature on the thermal conductivity was studied and it was found that the thermal conductivity of ceramic decreases with increasing in porosity and grain size. Therefore, it can be concluded that grain size and porosity are the dominant factors in the thermal conductivity. Although, thermal conductivity of ceramics can be affected by adding nano-particles, the grain boundaries which are unavoidable, play a significant role on thermal conductivity [45–47].

Diego et al. [37] studied the effects of thermal field in a turning cutting tool and used inversed problem to define thermal properties of coated WC. Coatings of TiN and Al_2O_3 were tested in thermal simulation. Both coated cutting tools showed higher temperatures than the uncoated one, and the amount of maximum temperature increased with coating thickness. They reported that TiN and Al_2O_3 coatings resulted in maximum temperature increase about 12.7 °C and 75.5 °C, respectively, in comparison with the uncoated WC [37]. Raju and Basu [48] added $TiSi_2$ (up to 10 wt%) to TiB_2 ceramic and analyzed the composite thermal properties. They showed that although the heat capacity increases versus temperature, the thermal conductivity of the composite decreases. At all investigated temperatures, the composite thermal conductivity and thermal diffusivity were higher than those of monolithic TiB_2 ceramic.

The aim of this research is to study the thermal diffusivity and microstructural evolution of spark plasma sintered TiB_2-30 vol% SiC composite with the addition of 5 wt% Ti as a sintering aid. To the best of our knowledge, this is the first time to investigate the fabrication and characterization of TiB_2—SiC—Ti composites. In addition, regarding the application of TiB_2 and its composites as tool materials, temperature distribution in a cutting tool is calculated by Finite Element Method (FEM) and temperature distribution along with maximum temperature points are studied.

2. Experimental procedure

2.1. Materials and processing

In this research, commercially available ceramic powders of TiB_2 (purity > 99.9%, particle size: 3–8 μm) and SiC (purity > 99%, particle size < 500 nm) were supplied by Xuzhou Hongwu Co. as the starting materials. Commercial metallic Ti powder (purity: 99.5%, particle size < 40 μm) was purchased from Alfa Aesar as the sintering aid. For preparation of the composite mixture, the Ti sinter additive (5 wt%) was supplemented to a mixture of TiB_2 (70 vol%) as the matrix and SiC (30 vol%) as the reinforcement phases. The mixture of TiB_2/SiC/Ti was mixed for 40 min in an ultrasonic bath using the ethanol as dispersing medium. The wet mixture of TiB_2—SiC—Ti composite was stirringly heated on a magnetic hot plate for 150 min at the temperature of 130 °C and completely dried in an oven for 24 h at 125 °C. After the drying process, the dehumidified powder mixture was crushed and moved through a sieve. At last, the as-mixed composite powder was poured into a cylindrical graphite die with an inner diameter of 30 mm. The consolidation process was conducted by a modern densification technique i.e. the spark plasma sintering. Hence, a SPS furnace (Nanozint 10i, Khala Poushan Felez Co., Iran) was employed to fabricate the composite sample at the maximum sintering temperature of 1900 °C for 7 min under 40 MPa external pressure in vacuum atmosphere ($\sim 5 \times 10^{-2}$ Pa).

2.2. Characterization

Bulk, theoretical and relative density calculations were fulfilled by the Archimedes principles and the rule of mixtures. Microstructural study on the polished and fracture surfaces of the as-sintered composite was carried out by the field emission scanning electron microscopy (Tescan Mira3). Chemical (elemental) and phase analyses were performed employing the energy dispersive spectroscopy (Oxford X-Max 80) and the X–ray diffractometry (Philips PW1800), respectively. Thermodynamics investigation for assessments of probable chemical reactions between the components, during the sintering process, was done using the HSC Chemistry (version 5.11) package. Thermal diffusivity of the sample was measured using the laser flash technique (LASTEH-STRI-034). A laser pulse heats one side of the sample, temperature sensors on the other side detect the heat and the transient temperature field is determined. As a function of the time, which the temperature is sensed by the sensors, and using the calibrated formula of the apparatus, the thermal diffusivity of the sample is determined [49,50].

2.3. Numerical simulation

As mentioned before, the generated high temperatures, as a result of machining process, changes the microstructure and thermo-physical properties of cutting tools [38]. Direct temperature determination through the tool has its difficulties like the movement of the workpiece, the effect of embedded thermocouples on applied heat flux area and chip obstruction on the rake face. Computational methods are a beneficial way to obtain detailed thermomechanical information about the involved pieces of the machining process. Solving the governing equation of heat transfer by numerical methods like FEM gives temperature distribution especially in the tool-chip interface. Nevertheless, the numerical method will not give correct answers without knowing the right value of applied flux at the chip-tool interface. In the present work, heat flux defined by Brito et al. [51] has been used. The three-dimensional computational domain is shown in Fig. 1 which consists of a cutting tool, a shim, and AISI 1045 tool holder. The dimensions are regarded as [51].

The governing equation is the heat diffusion equation as following:

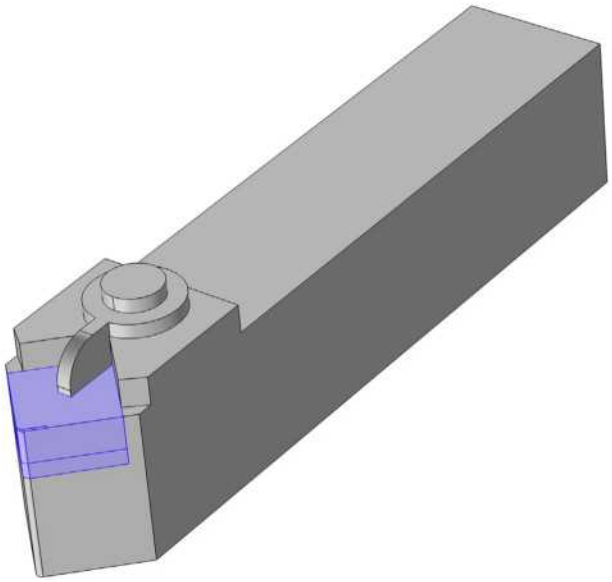

Fig. 1. Three-dimensional computational domain.

$$\frac{\partial(kT)}{\partial x} + \frac{\partial(kT)}{\partial y} + \frac{\partial(kT)}{\partial z} = \rho C \frac{\partial T}{\partial t} \quad (1)$$

where k is thermal conductivity, ρ is density and C is heat capacity of the materials. Since thermal conductivity and heat capacity are temperature dependent parameters, Eq. (1) is nonlinear. The governing equation is discretized by the Galerkin method and solved by FEM.

The considered domain is meshed by tetrahedral unstructured meshes which extremely fine elements is generated at the tool-chip interface (Fig. 2). The mesh independency is achieved at 69243 number of meshes.

The most important boundary condition is the applied heat flux at the interface of the tool-chip area which is as:

$$q'' = -k\frac{\partial T}{\partial z} \quad (2)$$

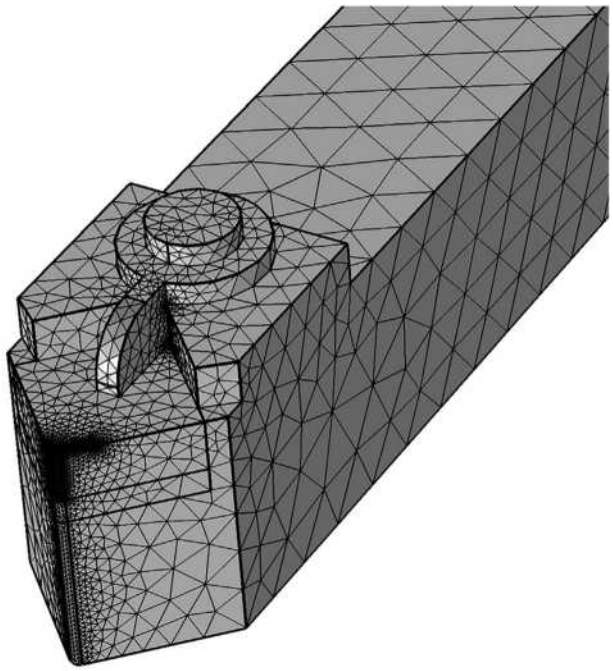

Fig. 2. A sample of mesh and cutting tool.

The surface area as well as applied flux value are essential considerations in the numerical investigation of cutting tool problems. The other boundaries, which are in contact with surrounded air, are cooled by natural convection and radiation [51]. The related boundary conditions are as follow:

$$-k\frac{\partial T}{\partial n} = h(T - T_\infty) + \sigma\varepsilon(T^4 - T_\infty^4) \quad (3)$$

where n is any direction, h is convective heat transfer coefficient, T_∞ is surrounding temperature, σ is the Stefan-Boltzmann constant and ε is surface emissivity. The natural convection heat transfer coefficients are chosen based on empirical correlations by Bergman et al. [52].

In the present work, the thermal contact resistance among the tool, the shim and the tool holder is taken into account as a 10-μm thick gap of air between the materials at 300 K. The air thermal properties are considered as $k = 0.026\ Wm^{-1}K^{-1}$ and $\alpha = 22.5 \times 10^{-06} m^2 s^{-1}$ [53]. The initial temperature of species is considered to be the room temperature.

In the present work, experimental data of heat fluxes by Brito et al. [51] is applied at the tool-chip interface and considering the mentioned boundary conditions, the temperature distribution through the domain is obtained by solving the heat diffusion equation. In order to validate the obtained results, the maximum temperatures at different time steps are compared by data of [51]. They used WC for both the tool and the shim, which their temperature dependent thermal properties are obtained from Grzesik et al. [54].

In the next step, the tool and shim materials are replaced by the as-sintered TiB_2—SiC—Ti (TST) composite in this research work. Using the same values of heat fluxes and boundary conditions, the temperature distribution through the proposed material is determined and compared with the result of WC tools. The most important parameter in the numerical investigation is the maximum temperature value generated at the cutting edge. This temperature has a direct effect on lifespan and quality of the workpiece.

3. Results and discussion

The addition of Ti as a metallic sintering aid improved the densification behavior of TiB_2—SiC composite so that, a fully dense sample with a relative density of 99.7% was fabricated by SPS process. Secondary electron SEM fractographs of the as-sintered TiB_2—SiC—Ti composite are shown in Fig. 3. A fully progressed densification can be observed in these micrographs as no porosity is remained in the sintered sample. In addition, an excellent sinterability has been developed which can be comprehended from the complete joining of particles together, i.e. the starting powders and in-situ formed phases. Achieving a relatively fine-grained TiB_2 matrix microstructure not only can be attributed to the positive role of additives (SiC and Ti), but also to the short dwell time of SPS process at final sintering temperature.

If the Ti additive remains unreacted in its metallic form, it can experience the plastic deformation below its melting temperature of 1668 °C [55]. Such behavior assisted the rearrangement of ceramic particles (TiB_2 and SiC) as a densification mechanism before the final stage of sintering process. In addition, the densification was further promoted via the liquid phase sintering mechanism due to the liquefaction of Ti at the temperatures from 1668 °C to 1900 °C. The positive influence of Ti on the densification of ZrB_2—SiC composites was published by Purwar et al. [56] and Ghasali et al. [57]. However, it should be noted that the occurrence of these densification mechanism depends on the presence of part of Ti in its metallic form during the sintering process. In this purpose, performing an XRD analysis from the as-sintered TiB_2—SiC—Ti composite seems to be helpful.

Fig. 4 presents the X-ray diffraction pattern of spark plasma sintered Ti-doped TiB_2—SiC composite. Together with the diffraction peaks of TiB_2, SiC and Ti as the starting materials, TiB, TiC and $TiSi_2$ phases were detected by XRD test as the in-situ formed Ti-containing compounds

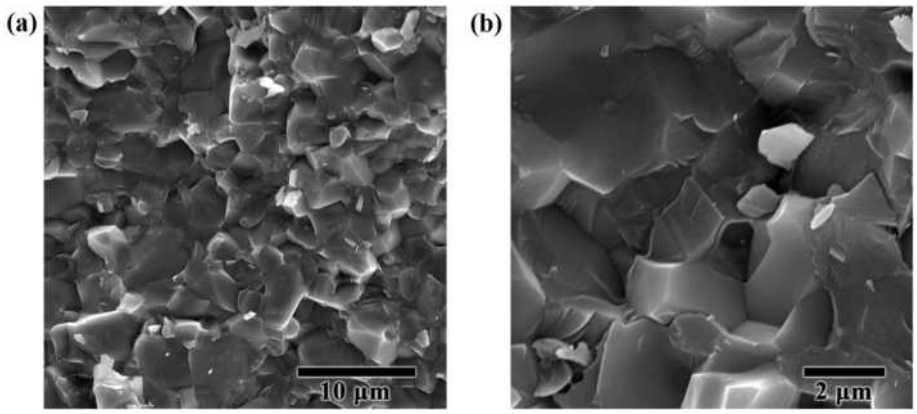

Fig. 3. (a) Low- and (b) high-magnification secondary electron SEM micrographs of the fracture surface of as-sintered TST composite.

during the sintering process. Despite the low amount of Ti in the initial powder mixture (5 wt%), the identification of elemental Ti along with TiB, TiC and $TiSi_2$ by XRD verifies the partially participation of Ti in chemical reactions that resulted in the formation of titanium boride, carbide and disilicide. The formation of refractory phases of TiB with a melting point of 2190 °C [58] and TiC with a melting point of 3160 °C [45] was proved in TiB_2–Ti [59,60] and TiB_2–SiC systems [35,61–63], respectively. Similar to the role of metallic Ti, the in-situ formed $TiSi_2$ with a melting point of 1540 °C [64] can assist the densification via liquid phase sintering mechanism.

In this section, the thermodynamic possibility of favorable chemical reactions in TiB_2–SiC–Ti system during the sintering process at the temperatures from 0 °C to 1900 °C is discussed. The investigated chemical reactions are chosen to be consistent with the results of XRD analysis. The thermodynamic assessments are carried out through the Gibbs free energy calculations employing the HSC Chemistry package and the outcomes are presented in Fig. 5.

According to Eq. (4), the Ti additive may react with the TiB_2 matrix to form TiB. Since the ΔG of Eq. (4) is negative (varies between −60 kJ and −40 kJ) at all temperature levels of sintering process, this reaction is thermodynamically favorable. The formation of TiB is verified by XRD test, because four peaks of titanium boride were detected.

$$TiB_2 + Ti = 2TiB \quad (4)$$

The metallic Ti can also react with the SiC reinforcement, in accord with the chemical reaction of Eq. (5) with ΔG variations between −100 kJ and −120 kJ, which leads to the formation of TiC and Si. The thermodynamic assessments revealed that the reaction of Ti with the SiC is more favorable than the TiB_2 because of more ΔG negativity of Eq. (5) than that of Eq. (4), as displayed in Fig. 5. The in-situ formation of TiC as a sinter product is also confirmed by XRD results presented in Fig. 4.

$$SiC + Ti = TiC + Si \quad (5)$$

The formation of TiC is verified by both thermodynamic and XRD analyses. Although Eq. (5) predicts the formation of Si along with TiC, such a phase is not seen in the XRD pattern (Fig. 4). Hence, the elemental Si which has formed based on the reaction of Eq. (5) seems to be completely consumed in another chemical reaction. Regarding the detection of $TiSi_2$ in the XRD spectrum, the in-situ formed Si, according to Eq. (5), can react with the residue of Ti via the pathway of Eq. (6). As it can be seen in Fig. 5, this reaction is also possible based on the thermodynamics. Similar chemical reactions were reported for the spark plasma sintered ZrB_2–SiC–Ti composite [57].

$$Ti + 2Si = TiSi_2 \quad (6)$$

Fig. 6 shows the low-magnification SEM micrograph (backscattered mode) of the polished surface of Ti-doped TiB_2–SiC composite and corresponding EDS maps of Ti, B, Si, C and O elements. Three distinctive regions are seen in Fig. 6a:

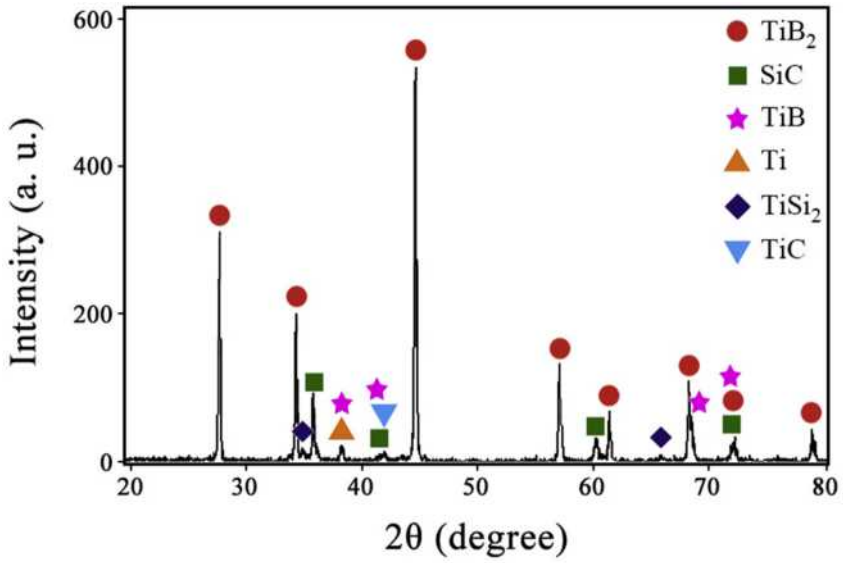

Fig. 4. XRD pattern of TST composite after sintering process disclosing the in-situ synthesize compounds.

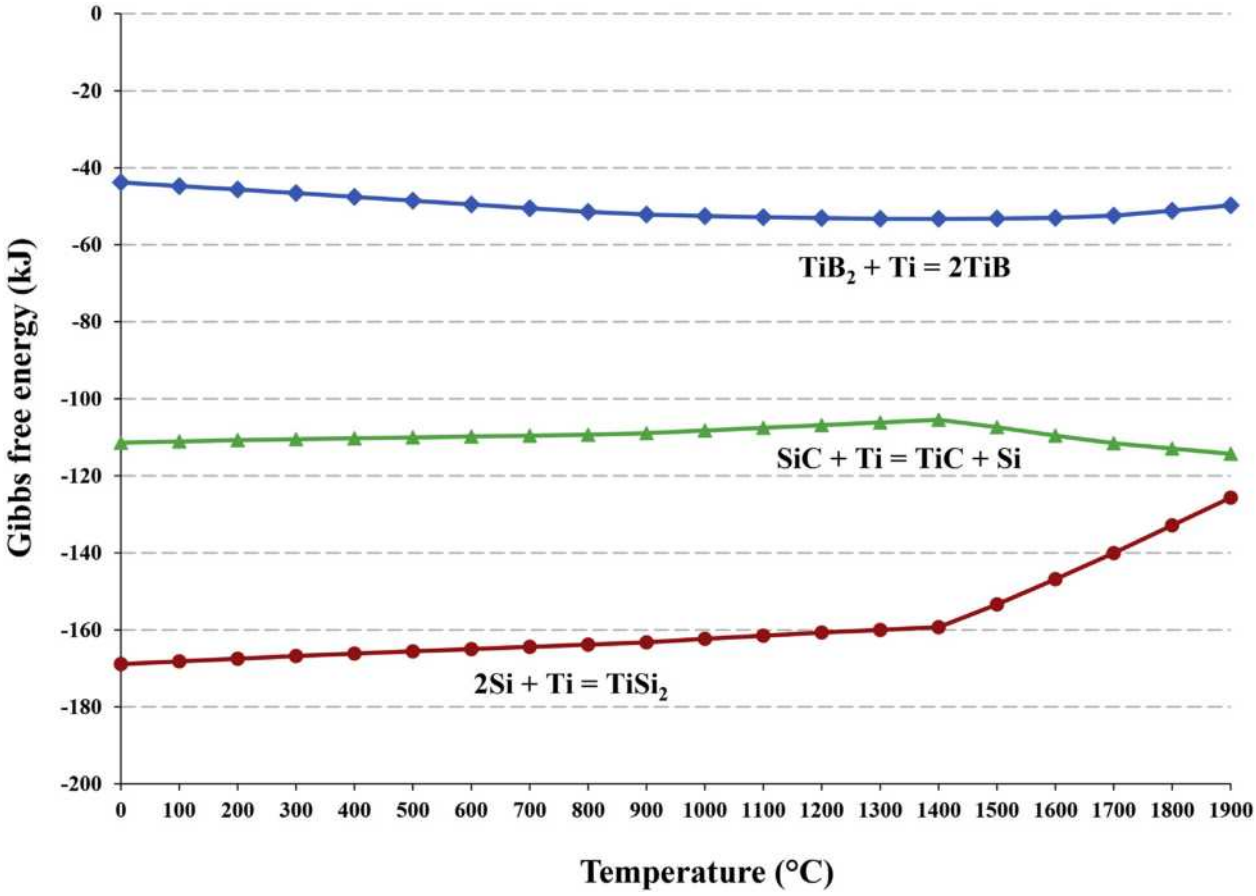

Fig. 5. Standard Gibbs free energy of thermodynamically favorable reactions in TST system.

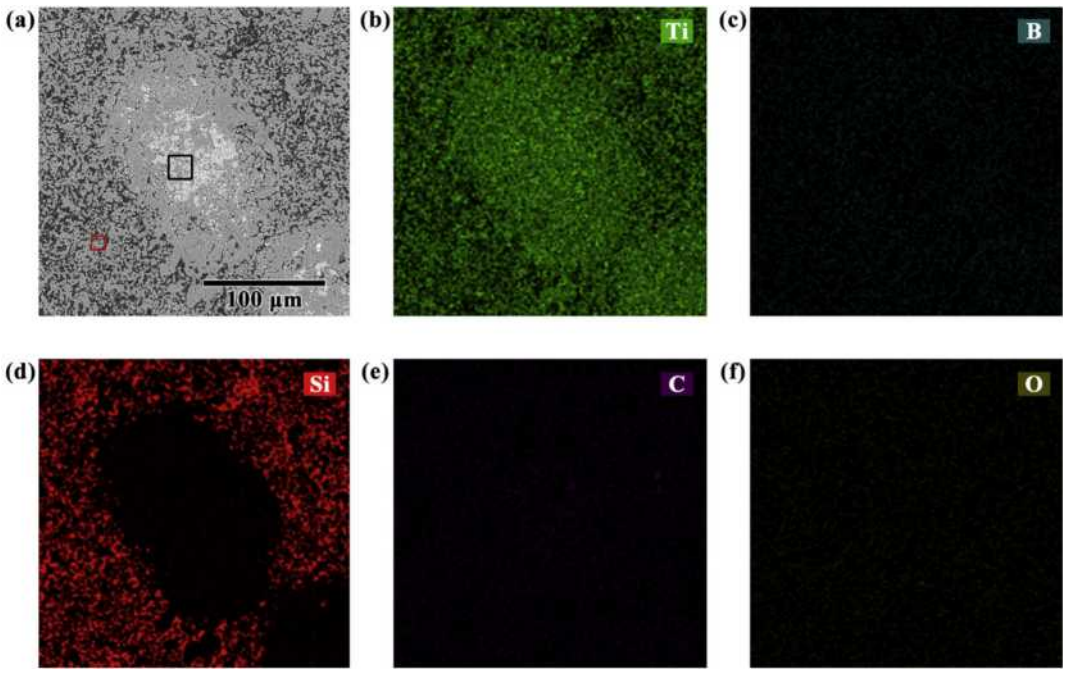

Fig. 6. (a) Backscattered SEM micrograph of the polished surface of as-sintered TST composite and (b–f) corresponding EDS maps of Ti/B/Si/C/O elements.

(1) The elliptical area, with an approximate 50-µm diameter, at the center of SEM image which contains a mixture of lightgray and darkgray phases.
(2) The darkgray-colored corona, with an approximate 30-µm width, around the elliptical area.
(3) The matrix area which includes a mixture of darkgray and dimgray phases.

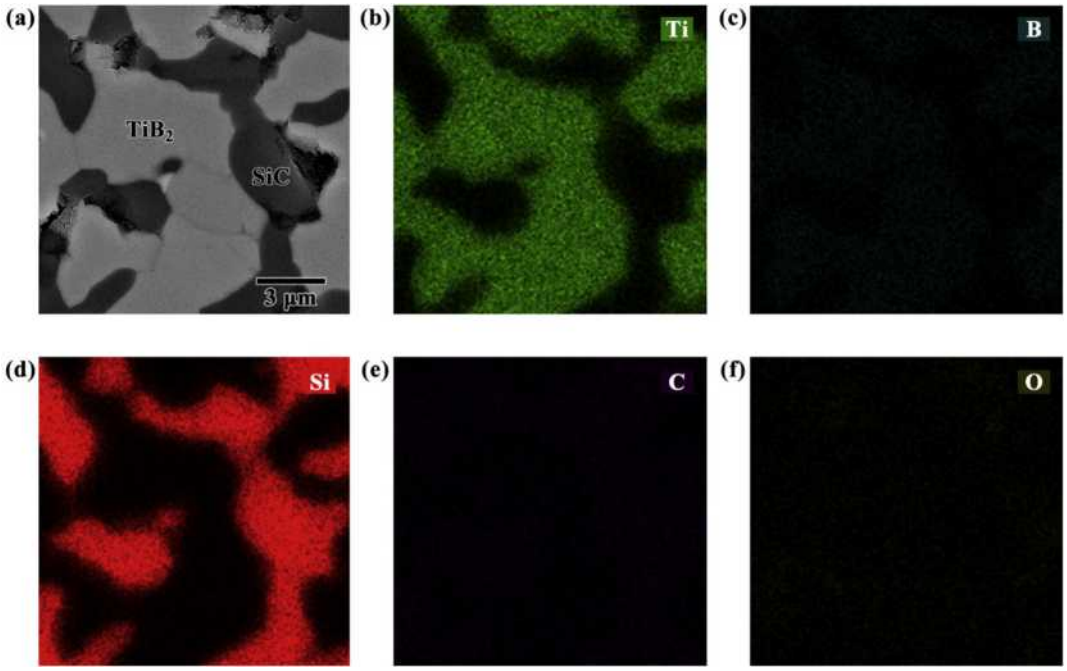

Fig. 7. (a) Closer view of Fig. 6a indicated by the red-outline square and (b–f) corresponding EDS maps of Ti/B/Si/C/O elements. (For interpretation of the references to color in this figure legend, the reader is referred to the Web version of this article.)

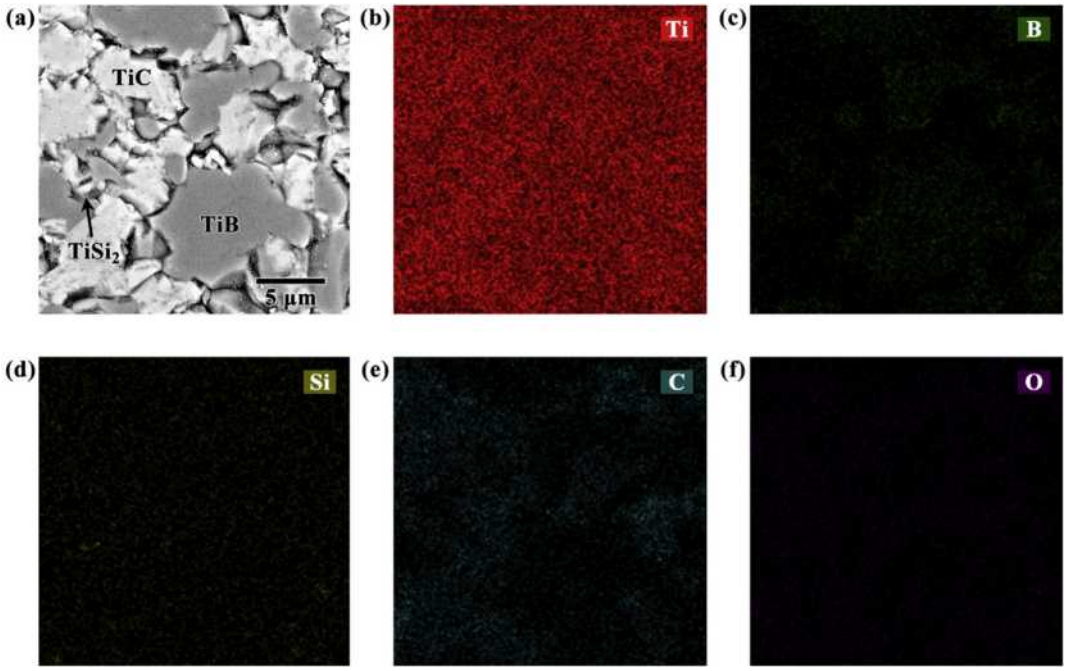

Fig. 8. (a) Closer view of Fig. 6a indicated by the black-outline square and (b–f) corresponding EDS maps of Ti/B/Si/C/O elements.

The size of elliptical area (~50 μm) is almost equal to the size of starting Ti particles (< 40 μm). The EDS analysis verifies that the elliptical area is rich in Ti (Fig. 6b) but free of Si (Fig. 6d). Hence, regarding the XRD results presented in Fig. 4 that area can be a mixture of unreacted Ti and/or the in-situ formed Ti-containing compounds such as TiB and TiC. The corona around the elliptical area seems to be formed due to the chemical reactions of Ti particle with the other composite constituents, i.e. TiB_2 (Eq. (4)) and/or SiC (Eq. (5)). On one hand, the corona is a monophasic region on the basis of its microstructural feature (Fig. 6a). On the other hand, similar to the elliptical area, the corona is a Si-free and Ti-rich area, based on the EDS maps (Fig. 6b, d). Therefore, it can be concluded that the corona is composed of TiB, namely, the product of chemical reaction between Ti and TiB_2. The matrix area is rich in both Ti and Si, but without a clear overlap between these elements. Concerning the composition of initial powder mixture and XRD analysis, such area seems to be composed of TiB_2 and SiC phases. The details of microstructural characterizations are discussed in the following paragraphs.

A high-magnification SEM micrograph from the area marked by a red-outline square in Fig. 6a (the matrix area) alongside its corresponding EDS elemental maps of Ti, B, Si, C and O are shown in Fig. 7. The darkgray-colored grains are rich in Ti (Fig. 7b) and B (Fig. 7c) and

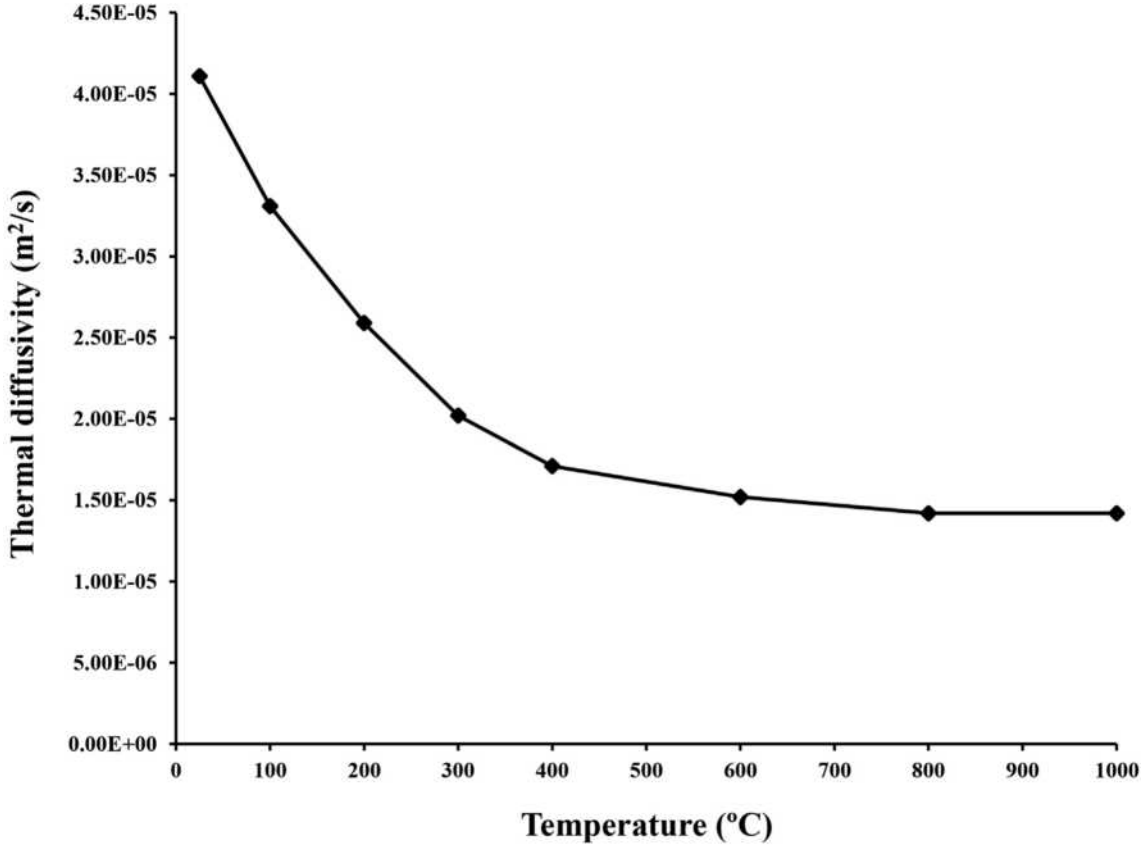

Fig. 9. Thermal diffusivity of TST composite at different temperatures.

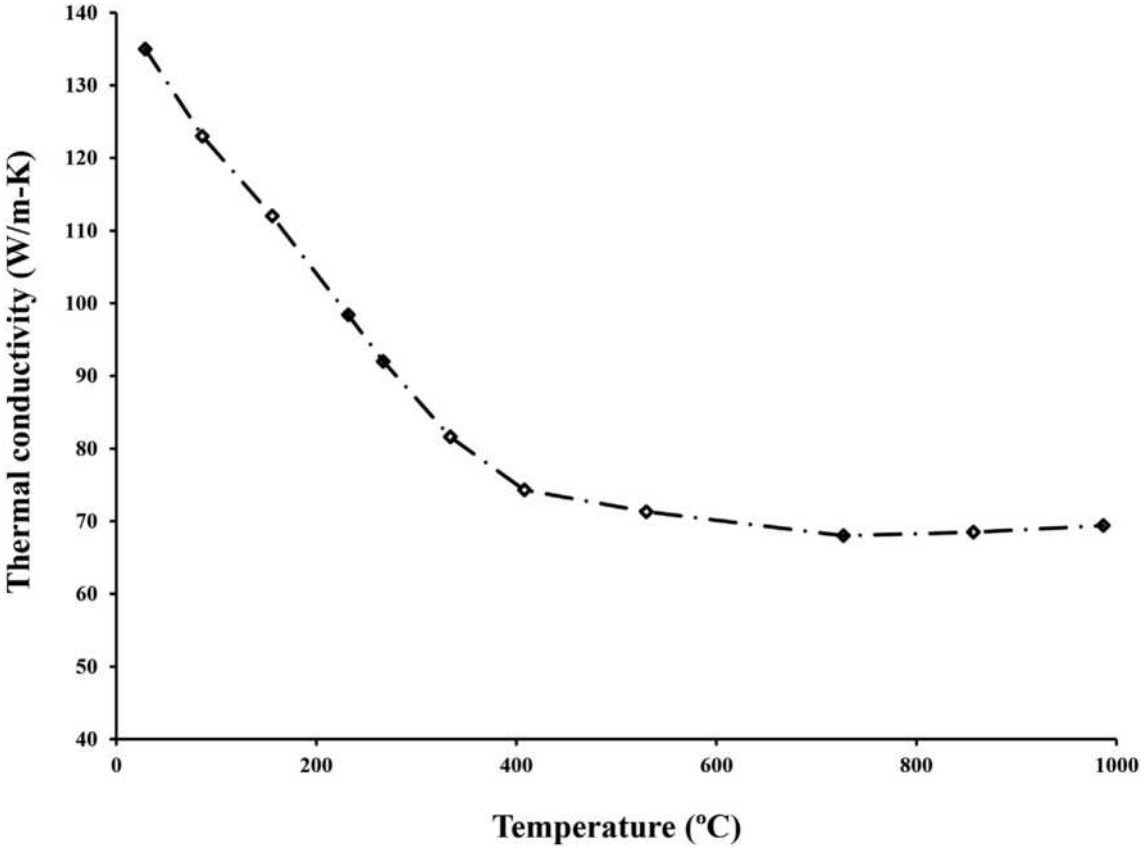

Fig. 10. Thermal conductivity of TST composite at different temperatures.

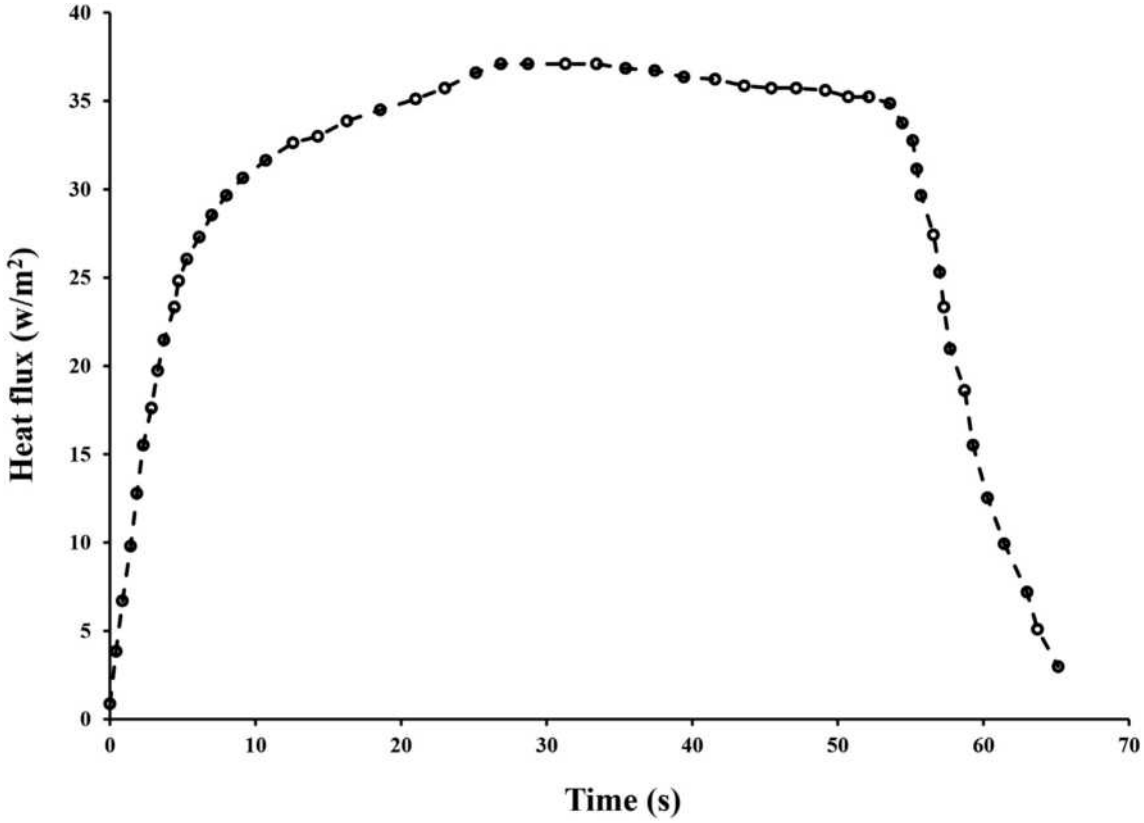

Fig. 11. Applied heat flux by Brito et al. [51].

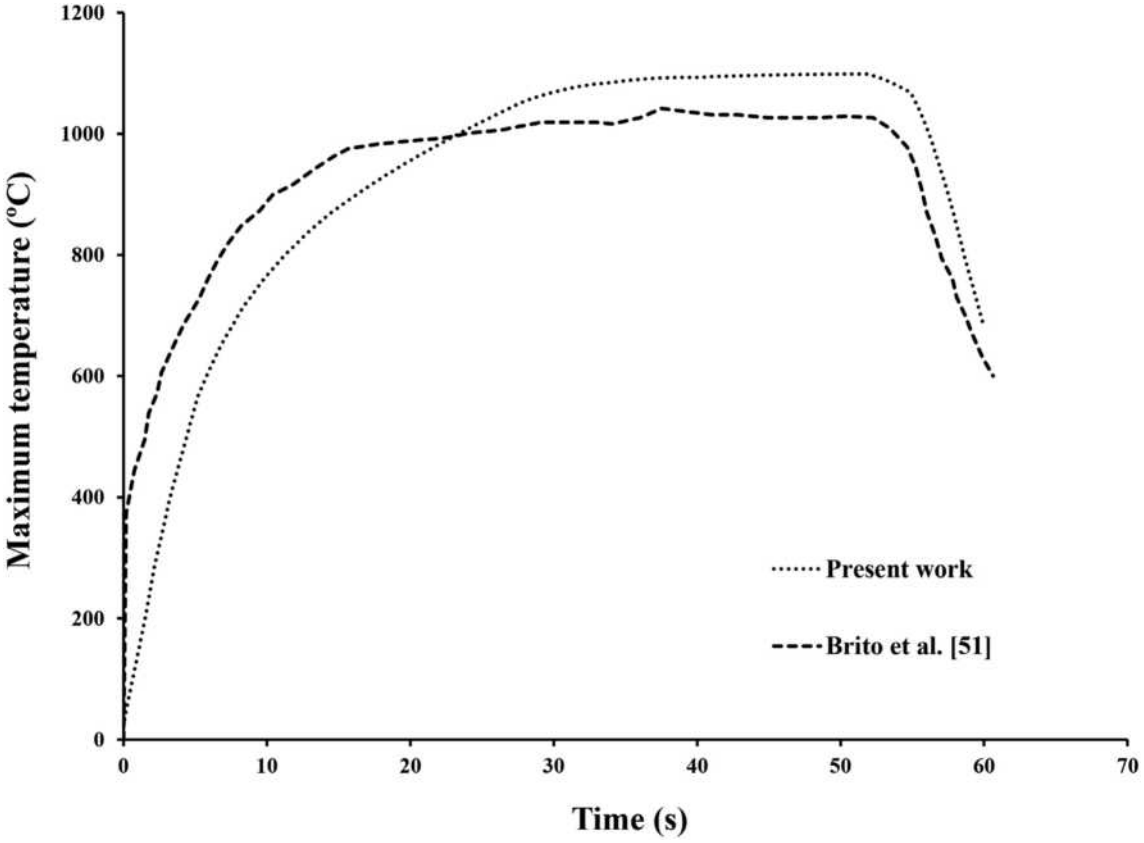

Fig. 12. Comparison of the maximum temperature of cutting tool.

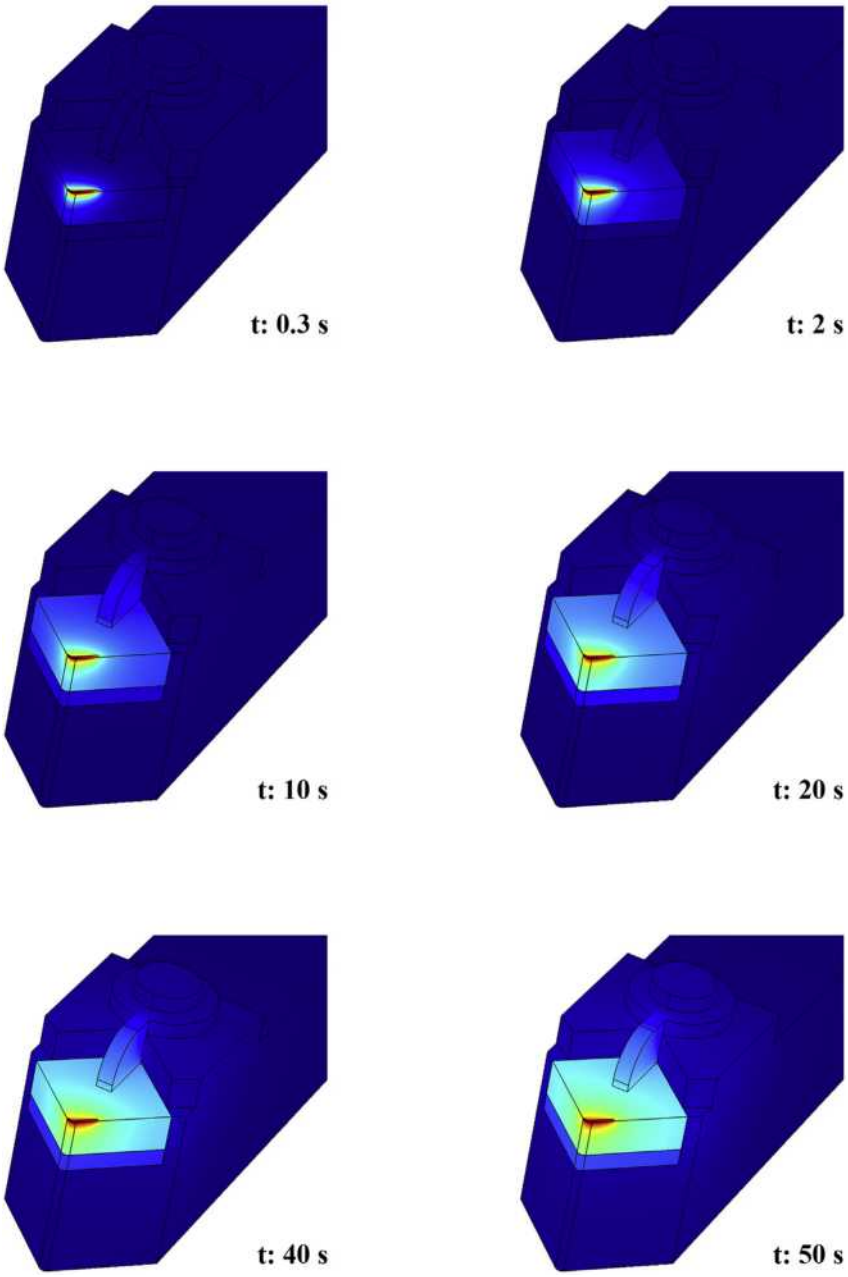

Fig. 13. Temperature distribution in TST composite as a cutting tool at different time steps.

can be attributed to the TiB_2. The Si-rich regions (Fig. 7d) are matched with the dimgray-colored phases (Fig. 7a) and can be related to the SiC reinforcement. A homogeneous distribution of SiC phases between the TiB_2 grains is clearly observed in the SEM image (Fig. 7a). Since there is no obvious overlap between the EDS maps of Ti (Fig. 7b) and Si (Fig. 7d) as well as regarding the formation of clean interfaces between Ti and Si particles in Fig. 7a, it seems that no chemical reactions has been occurred during the sintering process in the matrix area.

Fig. 8 displays another high-magnification SEM micrograph from the area marked by a black-outline square in Fig. 6a (the elliptical area) together with the corresponding EDS maps of Ti, B, Si, C and O elements. The selected square in Fig. 6a is located inside an area which previously belonged to a Ti particle. Such an area is poor in Si (Fig. 8d) and rich in Ti (Fig. 8b), hence, it can be attributed to the unreacted Ti as well as the Ti-based sinter product such as TiB and TiC phases, as already proved by XRD test. Since the lightgray-colored grains in Fig. 8a have considerable amounts of C (Fig. 8e), they can be nominated as TiC phase. The darkgray-colored grains are related to TiB due to the fact that such phases are rich in B element (Fig. 8c). According to Eq. (5), the TiC forms together with elemental Si, hence, it seems that the presence of Si at the grain boundaries of TiC is logical. Therefore, based on the reaction of Eq. (6), $TiSi_2$ can be in-situ formed around the TiC grains. Trace of $TiSi_2$, e.g. marked by an arrow in Fig. 8a, is seen in the SEM micrograph, however, the precise characterization of such black-colored interfacial phase needs the advanced instruments such as transmission electron microscopes (TEM).

Using laser flash technique, the thermal diffusivity of the TST composite was defined and shown in Fig. 9. Knowing the density and heat capacity, the thermal conductivity was calculated and shown in Fig. 10. It is concluded that thermal diffusivity and conductivity of the TST composite is a decreasing function of temperature as TiB_2. Thermal diffusivity of the TST composite is highly sensitive to temperature at first, but with increasing temperature, the sensitivity considerably reduces so that at higher temperatures, thermal diffusivity is

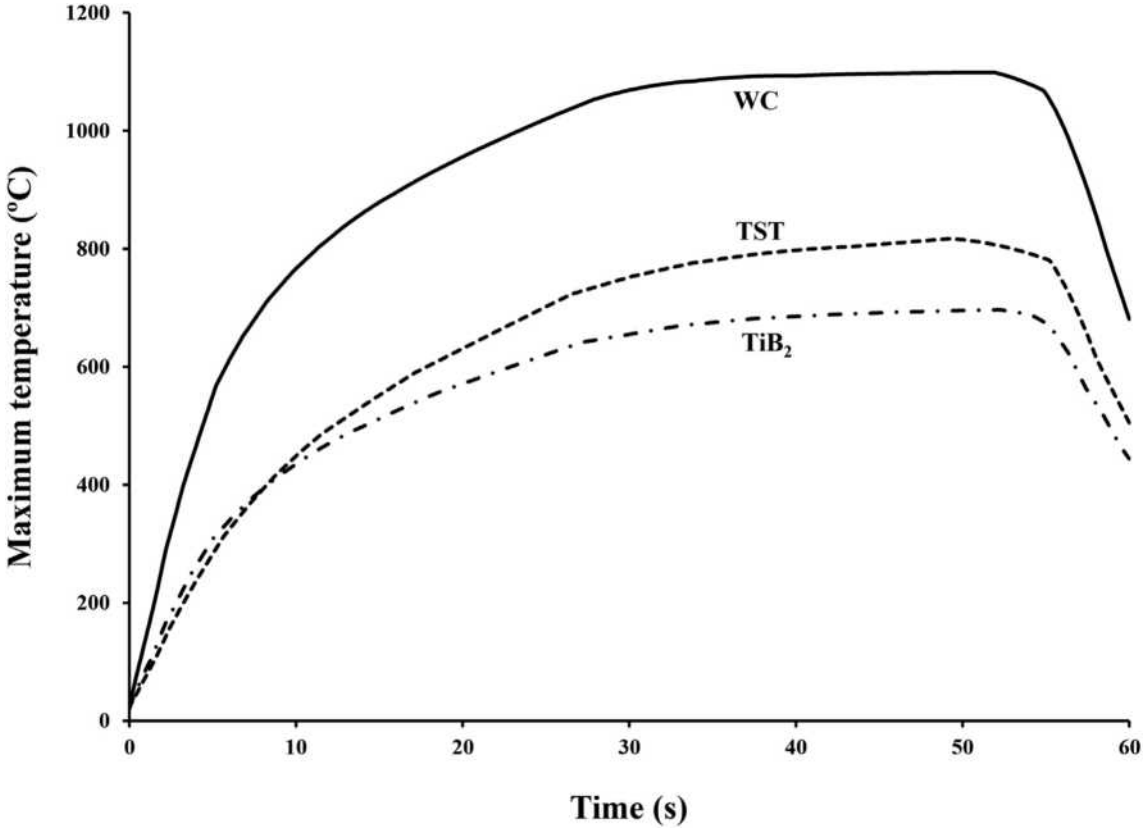

Fig. 14. Maximum temperature in the cutting tools with various materials at different time steps.

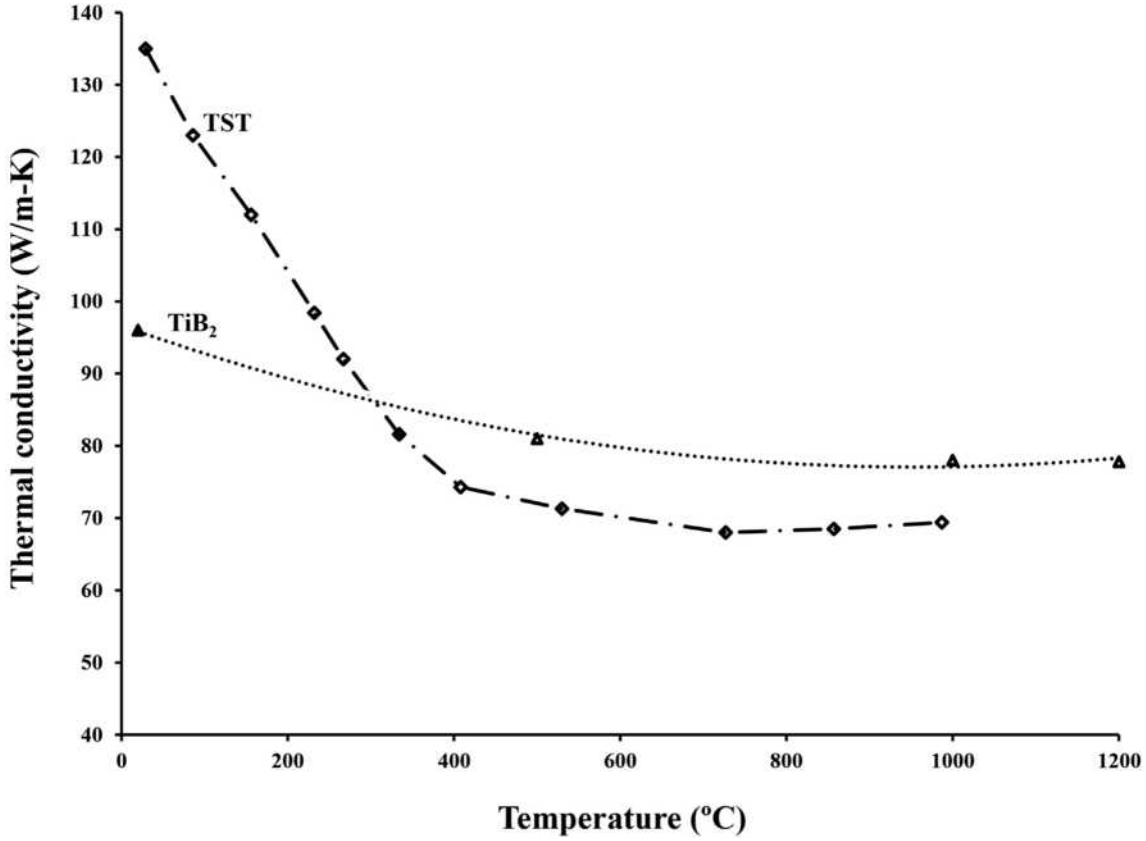

Fig. 15. Thermal conductivity of TiB_2 and TST versus temperature.

approximately constant. A same trend is observed for the thermal conductivity.

Since TiB_2 and its composites are often used as a hard material for cutting tools, the temperature distribution in a cutting tool-shaped TiB_2-based composites is investigated numerically. To ensure that the numerical results are reliable, at first the material of cutting tool was assumed to be WC and the obtained numerical results were compared with the experimental results of Brito et al. [51]. In this study, the experimentally obtained heat flux by Brito et al. [51] (Fig. 11) is applied as boundary condition and the calculated maximum temperature of the cutting tool is compared with the experimental results in Fig. 12.

It can be concluded form Fig. 12 that there is a good agreement between numerical and experimental data, therefore, the numerical method is verified and can be used for other materials as cutting tool. After numerical method verification, a cutting tool with the TST composite material is investigated using the same boundary conditions and heat flux. Temperature distribution through the cutting tool for the TST composite is demonstrated in Fig. 13 at different time steps.

As shown in Fig. 13, the tip of the cutting tool has the maximum temperature where is the interface between the tool and specimen. Exerted heat flux at the tip of the cutting tool is distributed by the conduction mechanism through the tool as time spends. In Fig. 14, the maximum temperature of cutting tool versus time is presented. As it is obvious the WC has the maximum temperature which is considerably higher than the monolithic TiB_2 and TST composite. High temperatures have undesirable influence on the tool lifespan and cause thermal stress and subsequent strains which affect the workpiece quality. Since the TiB_2 shows lower maximum temperatures, it can be a good alternative for WC. The TST shows an interesting behavior, at first its maximum temperature is lower than that of TiB_2, but after t = 10s, its maximum temperature rises faster and is higher than that of TiB_2. To justify such a behavior, the thermal conductivity of TiB_2 and TST versus the temperature is shown in Fig. 15.

It can be concluded that the thermal conductivity of TST is higher than that of TiB_2 at lower temperatures, but when the temperature increases, the thermal conductivity of TiB_2 gets higher values than TST. In the monolithic TiB_2, the temperature rising results in grain growth and the thermal resistivity of grain boundaries reduces, while in the TST composite, the grains cannot grow as simple as the monolithic TiB_2 because SiC, Ti, TiB, $TiSi_2$ and TiC particles inhibits the extreme grain growth. It should be noted that the thermal resistivity of grain boundaries has a significant effect on the thermal conductivity.

4. Conclusions

Metallic Ti (5 wt%) was selected as a sintering aid in a TiB_2 matrix composite with 30 vol% SiC as a reinforcement. A fully dense TiB_2−SiC−Ti (TST) composite was manufactured by spark plasma sintering at 1900 °C in vacuum under pressure of 35 MPa for 6 min. The thermal diffusivity, microstructural development and phase evolution of as-sintered TiB_2−SiC−Ti composite were scrutinized by laser flash, FESEM/EDS and XRD methods. The partially consumption of Ti during the sintering process and the in-situ synthesis of TiB, TiC and $TiSi_2$ compounds resulted in a promoted densification in TiB_2−SiC composite. A set of numerical investigations was carried out to determine the temperature distribution through a cutting tool. Both monolithic TiB_2 and TST composite show lower maximum temperature than WC. TiB_2 has lower maximum temperature than TST. Since grain growth of monolithic TiB_2 occurs faster than TST composite, it has lower thermal resistivity at higher temperatures in comparison with the composite.

References

[1] B. Mohammadpour, Z. Ahmadi, M. Shokouhimehr, M. Shahedi Asl, Spark plasma sintering of Al-doped ZrB2–SiC composite, Ceram. Int. 45 (4) (2019) 4262–4267.

[2] A. Sabahi Namini, Z. Ahmadi, A. Babapoor, M. Shokouhimehr, M. Shahedi Asl, Microstructure and thermomechanical characteristics of spark plasma sintered TiC ceramics doped with nano-sized WC, Ceram. Int. 45 (2) (2019) 2153–2160.

[3] Y. Azizian-Kalandaragh, A.S. Namini, Z. Ahmadi, M. Shahedi Asl, Reinforcing effects of SiC whiskers and carbon nanoparticles in spark plasma sintered ZrB2 matrix composites, Ceram. Int. 44 (16) (2018) 19932–19938.

[4] M. Shahedi Asl, B. Nayebi, Z. Ahmadi, S. Parvizi, M. Shokouhimehr, A novel ZrB2–VB2–ZrC composite fabricated by reactive spark plasma sintering, Mater. Sci. Eng., A 731 (2018) 131–139.

[5] M. Shahedi Asl, B. Nayebi, M. Shokouhimehr, TEM characterization of spark plasma sintered ZrB2–SiC–graphene nanocomposite, Ceram. Int. 44 (13) (2018) 15269–15273.

[6] M. Shahedi Asl, A statistical approach towards processing optimization of ZrB2–SiC–graphite nanocomposites. Part I: relative density, Ceram. Int. 44 (6) (2018) 6935–6939.

[7] I. Farahbakhsh, Z. Ahmadi, M. Shahedi Asl, Densification, microstructure and mechanical properties of hot pressed ZrB2–SiC ceramic doped with nano-sized carbon black, Ceram. Int. 43 (11) (2017) 8411–8417.

[8] Z. Ahmadi, B. Nayebi, M. Shahedi Asl, M. Ghassemi Kakroudi, I. Farahbakhsh, Sintering behavior of ZrB2–SiC composites doped with Si3N4: a fractographical approach, Ceram. Int. 43 (13) (2017) 9699–9708.

[9] K. Farhadi, A. Sabahi Namini, M. Shahedi Asl, A. Mohammadzadeh, M. Ghassemi Kakroudi, Characterization of hot pressed SiC whisker reinforced TiB2 based composites, Int. J. Refract. Metals Hard Mater. 61 (2016) 84–90.

[10] Z. Balak, M. Shahedi Asl, M. Azizieh, H. Kafashan, R. Hayati, Effect of different additives and open porosity on fracture toughness of ZrB2–SiC-based composites prepared by SPS, Ceram. Int. 43 (2) (2017) 2209–2220.

[11] M. Shahedi Asl, M. Ghassemi Kakroudi, Characterization of hot-pressed graphene reinforced ZrB2–SiC composite, Mater. Sci. Eng., A 625 (2015) 385–392.

[12] M. Shahedi Asl, M.G. Kakroudi, I. Farahbakhsh, B. Mazinani, Z. Balak, Synergetic effects of SiC and Csf in ZrB2-based ceramic composites. Part II: grain growth, Ceram. Int. 42 (16) (2016) 18612–18619.

[13] M. Shahedi Asl, F. Golmohammadi, M. Ghassemi Kakroudi, M. Shokouhimehr, Synergetic effects of SiC and Csf in ZrB2-based ceramic composites. Part I: densification behavior, Ceram. Int. 42 (3) (2016) 4498–4506.

[14] B. Nayebi, M. Shahedi Asl, M. Ghassemi Kakroudi, I. Farahbakhsh, M. Shokouhimehr, Interfacial phenomena and formation of nano-particles in porous ZrB2–40 vol% B4C UHTC, Ceram. Int. 42 (15) (2016) 17009–17015.

[15] M. Shahedi Asl, A. Sabahi Namini, M. Ghassemi Kakroudi, Influence of silicon carbide addition on the microstructural development of hot pressed zirconium and titanium diborides, Ceram. Int. 42 (4) (2016) 5375–5381.

[16] B. Nayebi, M. Shahedi Asl, M. Ghassemi Kakroudi, M. Shokouhimehr, Temperature dependence of microstructure evolution during hot pressing of ZrB2–30vol.% SiC composites, Int. J. Refract. Metals Hard Mater. 54 (2016) pp. 7–13.

[17] M. Shahedi Asl, B. Nayebi, Z. Ahmadi, P. Pirmohammadi, M. Ghassemi Kakroudi, Fractographical characterization of hot pressed and pressureless sintered SiAlON-doped ZrB2–SiC composites, Mater. Char. 102 (2015) 137–145.

[18] Z. Ahmadi, B. Nayebi, M. Shahedi Asl, M. Ghassemi Kakroudi, Fractographical characterization of hot pressed and pressureless sintered AlN-doped ZrB2–SiC composites, Mater. Char. 110 (2015) 77–85.

[19] M. Shahedi Asl, M. Ghassemi Kakroudi, A processing-microstructure correlation in ZrB2–SiC composites hot-pressed under a load of 10 MPa, Univers. J. Mater. Sci. 3 (1) (2015) 14–21.

[20] M. Shahedi Asl, B. Nayebi, Z. Ahmadi, M. Jaberi Zamharir, M. Shokouhimehr, Effects of carbon additives on the properties of ZrB2–based composites: a review, Ceram. Int. 44 (7) (2018) 7334–7348.

[21] M. Shahedi Asl, M. Ghassemi Kakroudi, R. Abedi Kondolaji, H. Nasiri, Influence of graphite nano-flakes on densification and mechanical properties of hot-pressed ZrB2–SiC composite, Ceram. Int. 41 (4) (2015) 5843–5851.

[22] S. Parvizi, Z. Ahmadi, M.J. Zamharir, M. Shahedi Asl, Synergistic effects of graphite nano-flakes and submicron SiC particles on the characteristics of spark plasma sintered ZrB2 nanocomposites, Int. J. Refract. Metals Hard Mater. 75 (2018) 10–17.

[23] M. Shahedi Asl, Microstructure, hardness and fracture toughness of spark plasma sintered ZrB2–SiC–Cf composites, Ceram. Int. 43 (17) (2017) 15047–15052.

[24] Z. Hamidzadeh Mahaseni, M. Dashti Germi, Z. Ahmadi, M. Shahedi Asl, Microstructural investigation of spark plasma sintered TiB2 ceramics with Si3N4 addition, Ceram. Int. 44 (11) (2018) 13367–13372.

[25] M. Dashti Germi, Z. Hamidzadeh Mahaseni, Z. Ahmadi, M. Shahedi Asl, Phase evolution during spark plasma sintering of novel Si3N4-doped TiB2–SiC composite, Mater. Char. 145 (2018) 225–232.

[26] M. Shahedi Asl, M.J. Zamharir, Z. Ahmadi, S. Parvizi, Effects of nano-graphite content on the characteristics of spark plasma sintered ZrB2–SiC composites, Mater. Sci. Eng., A 716 (2018) 99–106.

[27] M. Shahedi Asl, M. Ghassemi Kakroudi, B. Nayebi, A fractographical approach to the sintering process in porous ZrB2–B4C binary composites, Ceram. Int. 41 (1) (2015) 379–387.

[28] F. Shayesteh, S.A. Delbari, Z. Ahmadi, M. Shokouhimehr, M. Shahedi Asl, Influence of TiN dopant on microstructure of TiB2 ceramic sintered by spark plasma, Ceram. Int. (2018), https://doi.org/10.1016/j.ceramint.2018.11.228.

[29] A. Sabahi Namini, A. Motallebzadeh, B. Nayebi, M. Shahedi Asl, M. Azadbeh, Microstructure–mechanical properties correlation in spark plasma sintered Ti–4.8 wt.% TiB2 composites, Mater. Chem. Phys. 223 (2019) 789–796.

[30] S.A. Delbari, B. Nayebi, E. Ghasali, M. Shokouhimehr, M. Shahedi Asl, Spark plasma sintering of TiN ceramics codoped with SiC and CNT, Ceram. Int. 45 (3) (2019) 3207–3216.

[31] M. Akhlaghi, S.A. Tayebifard, E. Salahi, M. Shahedi Asl, Spark plasma sintering of TiAl–Ti3AlC2 composite, Ceram. Int. 44 (17) (2018) 21759–21764.

[32] Z. Balak, M. Azizieh, H. Kafashan, M. Shahedi Asl, Z. Ahmadi, Optimization of effective parameters on thermal shock resistance of ZrB2-SiC-based composites prepared by SPS: using Taguchi design, Mater. Chem. Phys. 196 (2017) 333–340.
[33] A.L. Chamberlain, W.G. Fahrenholtz, G.E. Hilmas, D.T. Ellerby, High-strength zirconium diboride-based ceramics, J. Am. Ceram. Soc. 87 (6) (2004) 1170–1172.
[34] W.G. Fahrenholtz, Thermodynamic analysis of ZrB 2 ?SiC oxidation: formation of a SiC-depleted region, J. Am. Ceram. Soc. 90 (1) (2007) 143–148.
[35] M. Shahedi Asl, I. Farahbakhsh, B. Nayebi, Characteristics of multi-walled carbon nanotube toughened ZrB2–SiC ceramic composite prepared by hot pressing, Ceram. Int. 42 (1) (2016) 1950–1958.
[36] M. Shahedi Asl, M. Ghassemi Kakroudi, F. Golestani-Fard, H. Nasiri, A Taguchi approach to the influence of hot pressing parameters and SiC content on the sinterability of ZrB2-based composites, Int. J. Refract. Metals Hard Mater. 51 (2015) 81–90.
[37] D.C. Ferreira, E. dos S. Magalhães, R.F. Brito, S.M.M. Lima E Silva, Numerical analysis of the influence of coatings on a cutting tool using COMSOL, Int. J. Adv. Manuf. Technol. 97 (1–4) (2018) 1305–1314.
[38] M. Gostimirovic, P. Kovac, M. Sekulic, An inverse heat transfer problem for optimization of the thermal process in machining, Sadhana 36 (4) (2011) 489–504.
[39] G.B. Raju, B. Basu, A.K. Suri, Thermal and electrical properties of TiB2–MoSi2, Int. J. Refract. Metals Hard Mater. 28 (2) (2010) 174–179.
[40] N. Burger, A. Laachachi, M. Ferriol, M. Lutz, V. Toniazzo, D. Ruch, Review of thermal conductivity in composites: mechanisms, parameters and theory, Prog. Polym. Sci. 61 (2016) 1–28.
[41] R. Bahadori, H. Gutierrez, S. Manikonda, R. Meinke, Two-dimensional transient heat conduction in multi-layered composite media with temperature dependent thermal diffusivity using floating random walk Monte-Carlo method, Int. J. Heat Mass Tran. 115 (2017) 570–580.
[42] B. Todorović, T. Jokić, Z. Rakočević, Z. Marković, B. Gaković, T. Nenadović, The effect of rapid thermal annealing on structural and electrical properties of TiB2 thin films, Thin Solid Films 300 (1–2) (1997) 272–277.
[43] H. Yuan, J. Li, Q. Shen, L. Zhang, Preparation and thermal conductivity characterization of ZrB2 porous ceramics fabricated by spark plasma sintering, Int. J. Refract. Metals Hard Mater. 36 (2013) 225–231.
[44] S. Chakraborty, D. Debnath, A.R. Mallick, P.K. Das, Mechanical and thermal properties of hot pressed ZrB2 system with TiB2, Int. J. Refract. Metals Hard Mater. 46 (2014) 35–42.
[45] A. Babapoor, M. Shahedi Asl, Z. Ahmadi, A. Sabahi Namini, Effects of spark plasma sintering temperature on densification, hardness and thermal conductivity of titanium carbide, Ceram. Int. 44 (12) (2018) 14541–14546.
[46] J.W. Zimmermann, G.E. Hilmas, W.G. Fahrenholtz, R.B. Dinwiddie, W.D. Porter, H. Wang, Thermophysical properties of ZrB 2 and ZrB 2 –SiC ceramics, J. Am. Ceram. Soc. 91 (5) (2008) 1405–1411.
[47] W.T. Kwon, et al., Microstructures and thermal conductivities of reaction sintered SiC ceramics, Adv. Appl. Ceram. 113 (6) (2014) 328–333.
[48] B.R. Golla, B. Basu, Hot-pressed TiB2–10wt.% TiSi2 ceramic with extremely good thermal transport properties at elevated temperatures (up to 1273K), Scripta Mater. 68 (1) (2013) 79–82.
[49] Z. Aparna, M.M. Michael, S.K. Pabi, S. Ghosh, Diversity in thermal conductivity of aqueous Al 2 O 3 - and Ag-nanofluids measured by transient hot-wire and laser flash methods, Exp. Therm. Fluid Sci. 94 (2018) 231–245.
[50] L. Wang, M. Gandorfer, T. Selvam, W. Schwieger, Determination of faujasite-type zeolite thermal conductivity from measurements on porous composites by laser flash method, Mater. Lett. 221 (2018) 322–325.
[51] R.F. Brito, S.R. Carvalho, S.M.M. Lima E Silva, Experimental investigation of thermal aspects in a cutting tool using comsol and inverse problem, Appl. Therm. Eng. 86 (2015) 60–68.
[52] D.D. Bergman TL, A.S. Lavine, F.P. Incropera, Fundamentals of Heat and Mass Transfer, seventh ed., Wiley, New York, 2011.
[53] A.S.L.F.P. Incropera, D.P. DeWitt, T.L. Bergman, Fundamentals of Heat and Mass Transfer, sixth ed., John Wiley & Sons, USA, 2007.
[54] M.B.W. Grzesik, P. Niesłony, Modelling of the cutting process analytical and simulation methods, Adv. Manuf. Sci. Technol. 33 (2009) 5–29.
[55] M. Shahedi Asl, A. Sabahi Namini, A. Motallebzadeh, M. Azadbeh, Effects of sintering temperature on microstructure and mechanical properties of spark plasma sintered titanium, Mater. Chem. Phys. 203 (2018) 266–273.
[56] A. Purwar, R. Mukherjee, K. Ravikumar, S. Ariharan, N.K. Gopinath, B. Basu, Development of ZrB2–SiC–Ti by multi stage spark plasma sintering at 1600°C, J. Ceram. Soc. Japan 124 (4) (2016) 393–402.
[57] E. Ghasali, M. Shahedi Asl, Microstructural development during spark plasma sintering of ZrB2–SiC–Ti composite, Ceram. Int. 44 (15) (2018) 18078–18083.
[58] D. Galvan, V. Ocelík, Y. Pei, B.J. Kooi, J.T.M. De Hosson, E. Ramous, Microstructure and properties of TiB/Ti-6Al-4V coatings produced with laser treatments, J. Mater. Eng. Perform. 13 (4) (2004) 406–412.
[59] A. Sabahi Namini, M. Azadbeh, M. Shahedi Asl, Effects of in-situ formed TiB whiskers on microstructure and mechanical properties of spark plasma sintered Ti–B4C and Ti–TiB2 composites, Sci. Iran. 25 (2) (2018) 762–771.
[60] A. Sabahi Namini, M. Azadbeh, M. Shahedi Asl, Effect of TiB2 content on the characteristics of spark plasma sintered Ti–TiBw composites, Adv. Powder Technol. 28 (6) (2017) 1564–1572.
[61] Z. Ahmadi, B. Nayebi, M. Shahedi Asl, I. Farahbakhsh, Z. Balak, Densification improvement of spark plasma sintered TiB2-based composites with micron-, submicron- and nano-sized SiC particulates, Ceram. Int. 44 (10) (2018) 11431–11437.
[62] M. Shahedi Asl, Z. Ahmadi, S. Parvizi, Z. Balak, I. Farahbakhsh, Contribution of SiC particle size and spark plasma sintering conditions on grain growth and hardness of TiB2 composites, Ceram. Int. 43 (16) (2017) 13924–13931.
[63] A. Sabahi Namini, S.N. Seyed Gogani, M. Shahedi Asl, K. Farhadi, M. Ghassemi Kakroudi, A. Mohammadzadeh, Microstructural development and mechanical properties of hot pressed SiC reinforced TiB2 based composite, Int. J. Refract. Metals Hard Mater. 51 (2015) 169–179.
[64] J.G. Xu, C.C. Li, Synthesis of titanium disilicide by the 'chemical oven' self-propagating combustion method, Appl. Mech. Mater. 44–47 (2010) 2888–2891.